

pubs.acs.org/cm Article

Design of Dendritic Promesogenic Ligands for Liquid Crystal-Nanoparticle Hybrid Systems

Yifan Ning, Zhe Liu, Shengsong Yang, Yuma Morimitsu, Chinedum O. Osuji, and Christopher B. Murray*



Cite This: Chem. Mater. 2023, 35, 3532-3544



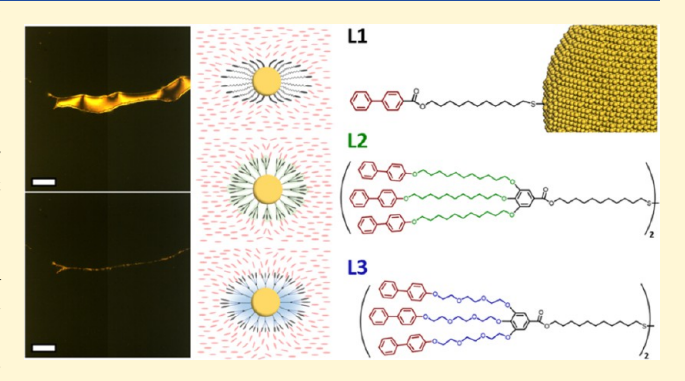
ACCESS I

III Metrics & More

Article Recommendations

s Supporting Information

ABSTRACT: Liquid crystal-nanoparticle (LC-NP) hybrid systems allow synergistic interactions between LC matrixes with anisotropic alignment and NP dopants with versatile functionalities. A uniform, well-dispersed, and highly stable thermotropic LC-NP mixture paves the way for further applications. In this work, a linear promesogenic ligand and two types of dendritic promesogenic ligands with alkyl or oligo ethylene glycol (OEG) chains are designed and synthesized to facilitate incorporating NPs into the thermotropic 4-cyano-4'-pentylbiphenyl (5CB) LC matrix. A comparison study between the linear and the dendritic ligands on the capability to promote miscibility and stability of NPs in LCs is conducted. Miscibility test results show that the linear ligand and the OEG-chained dendrimer both perform well in uniformly



dispersing NPs in LCs. Dynamic assemblies of NPs assisted by dendritic ligands and driven by aligning and equilibrating of mesogens are captured, showing the potential of manipulating the assembly of NPs through external thermal stimuli. The stability test shows that both types of dendrimers can significantly enhance the shelf-life time and thermal stability of NPs compared to the linear ligand. In particular, Au NPs capped with OEG-chained dendrimers are stable in 5CB for 6 months at room temperature and over 10 h at 50 °C. The synthesis of dendritic ligands is highly modulated and can be generalized onto NPs with different dimensions and properties. Tied by the dendritic promesogenic ligands, this LC-NP hybrid system with good uniformity and stability could be further applied to tunable optical displays, responsive materials, etc.

■ INTRODUCTION

Liquid crystals (LCs) as soft materials with unique supramolecular alignment have wide applications in optical devices and smart materials. 1-5 The LC-nanoparticle (NP) hybrid systems introduce a novel branch of metamaterials into the family of LCs.⁶⁻⁹ By engineering the combination of different LCs and NPs, a variety of functions from the NPs, such as optical, 10,11 electrical, 12 electro-optical, 13,14 thermal, 15 and magnetic properties, 16,17 can be brought in the LC matrixes. The interaction between the colloidal NP dopants and the anisotropic matrixes is also a special platform for manipulating the assembly of NPs and building up stimuli-responsive systems. 18-22 However, when LCs act as the matrix or the "solvents" unlike traditional isotropic solvents, such as toluene or chloroform, the intrinsic anisotropy makes it of great challenge to load NPs with decent uniformity, miscibility, and stability.²³⁻²⁶ Post-synthesis treatment and chemical decoration on the surface of NPs with (pro)mesogenic ligands are needed.²⁷⁻²⁹ For example, to facilitate the incorporation of NPs in the 4-cyano-4'-pentylbiphenyl (5CB) matrix, grafting biphenyl or cyanobiphenyl-derived (pro)mesogenic ligands at the NP surface is a commonly applied strategy. 30,31 However,

previous studies have shown that linear alkyl ligands fail to stabilize the NPs in organic solvents over an extended period.³² In the case of LCs, things could be worse as the depletion of equatorial ligands caused by the director of mesogens leaving the side of NPs unprotected and prone to aggregate.^{26,33,34} Nevertheless, there is still little research about the stability of this hybrid system, which greatly limits the development of potential applications.

Dendrimers are a group of molecules with branched, ordered, and compact structures.^{35–37} They are synthetically tunable scaffolds for adding various functionalities.^{38–42} When serving as ligands, their conical structure can be nicely fitted onto the NP surface and form a well-surrounded capping layer, preventing NPs from self-aggregating or being negatively influenced by external disturbance, which is very important for

Received: January 9, 2023 Revised: April 3, 2023 Published: April 19, 2023





NPs with problems in colloidal stability. 17,34,43,44 Previous studies have shown that using dendritic promesogenic ligands on $CoFe_2O_4$ NPs could help suspend magnetic NPs in 5CB, which is of great difficulty due to the magnetic interaction from the NPs themselves. 45,46 Besides achieving miscibility at room temperature, it is also critical to maintain the quality of NPs in thermotropic LCs under elevated temperatures; otherwise, aggregation and fusion of NPs during the heating and cooling cycles could bring difficulty in interpreting the data and reproducing the results. However, the mesophases of many LCs are quite above room temperature (Figure 1), whereas the performance and stability of NPs are usually very temperature sensitive, $^{47-50}$ bringing more challenges to prepare a uniform and stable LC-NP hybrid system.

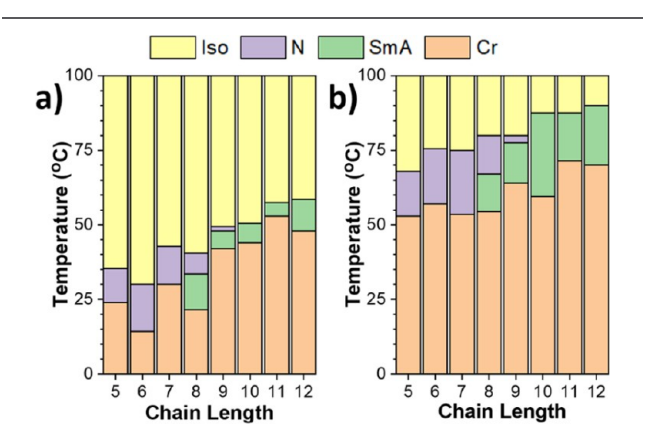


Figure 1. Phases of the cyanobiphenyl-derived LCs. (a) 5CB to 12CB. (b) 5OCB to 12OCB. Plotted with data extracted from a previous report. ⁵²

Previous work indicates that ligands with a more flexible molecular structure and less crystallinity could assist miscibility.^{24,51} In this paper, we take advantage of the dendritic promesogenic ligand capping to facilitate miscibility and increase the stability of NPs in the thermotropic LC matrix 5CB. Two types of biphenyl-functionalized dendritic promesogenic ligands with alkyl chains (L2 and L4) or oligo ethylene glycol (OEG) chains (L3 and L5) are designed, synthesized, and compared systematically with a linear biphenyl ligand (L1). The miscibility test characterized by polarized optical microscopy (POM) supports the design of using flexible OEG chains in dendritic structures. Dynamic assemblies of Au agglomerates assisted by dendrimers and driven by equilibration of the matrix are also captured. Tests on shelf life and thermal stability show that both types of dendritic ligands are more effective than the linear ligand in stabilizing Au NPs in 5CB, especially the OEG-chained dendrimers. The molecular arrangements of promesogenic ligands in different phases of 5CB, determined by their molecular structures and the alignment of matrix mesogens, are proposed based on the experimental results. The application of dendritic promesogenic ligands can be generalized to NPs with different sizes, shapes, materials, and properties, such as coreshell CdSe/CdS nanorods (NRs) and rare-earth Gd₂O₃ triangular nanoplatelets.

■ RESULTS AND DISCUSSION

Ligand Design and Synthesis. The motivation for designing dendritic promesogenic ligands to stabilize NPs in LCs is as follows: (1) a compact packing of the peripheral biphenyls can promote the interaction and penetration with the matrix mesogens to facilitate miscibility, (2) the unique cone shape of a dendrimer forms a denser organic corona around the NPs, avoiding NPs with strong interactions to

Scheme 1. Synthesis of the Promesogenic Ligands^a

a)

(HO
$$\frac{1}{9}$$
 s $\frac{1}{2}$ 1

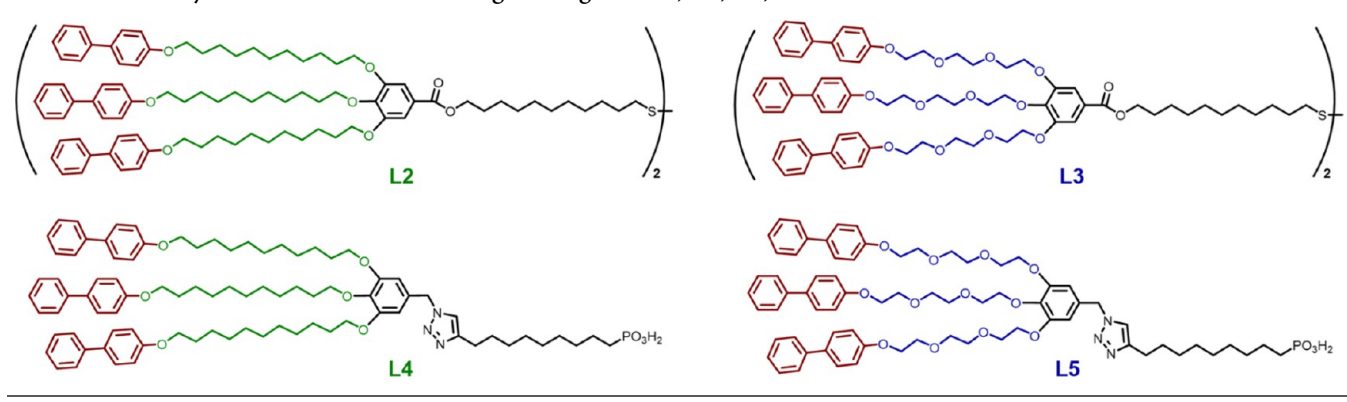
(B)

(HO $\frac{1}{9}$ s $\frac{1}{2}$ 1

(HO $\frac{1}{9}$ s \frac

"Reagents and conditions: (i) SOCl₂, anhydrous DCM, rt, 3 h; then 1, DMAP, triethylamine (TEA), anhydrous DCM, rt, 24 h. (ii) K₂CO₃, KI, DMF, 80 °C, overnight. (iii) TsCl, TEA, anhydrous DCM, rt, overnight. (iv) KOH, THF/H₂O/MeOH, reflux. (v) LiAlH₄, THF, 60 °C, 4 h. (vi) SOCl₂, anhydrous DCM, rt, 3 h. (vii) NaN₃, DMF, 80 °C, overnight. (viii) CuSO₄·SH₂O, sodium ascorbate, THF/H₂O, microwave, 65 °C, 40 h.

Scheme 2. Library of the Dendritic Promesogenic Ligands L2, L3, L4, and L5



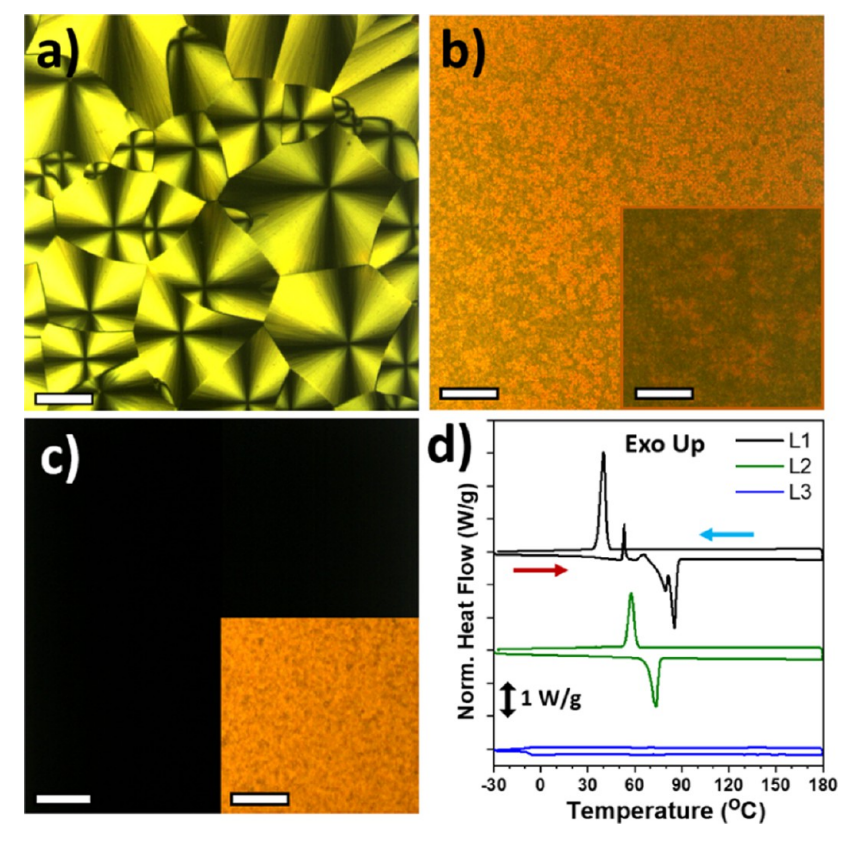


Figure 2. (a-c) POM images of L1, L2, and L3 at 25 °C with 90° crossed polarizers. The inset of (b) gives a zoom-in image of the fan-shaped texture of L2. All samples are sandwiched between two glass slices with a fixed gap of 60 μ m. The inset of (c) shows a bright-field image of L3. (d) Second cycle of heating (red arrow) and cooling (cyan arrow) in DSC of L1 (black), L2 (green), and L3 (blue). Scale bars: (a-c) and the inset of (c) 200 μ m and the inset of (b) 50 μ m.

aggregate, and (3) less deformation of the ligand corona prevents NPs from fusing and enhances their thermal stability,⁵³ which is important, especially when the mesophases move up to a higher temperature region or the characterization of this hybrid system takes an extended time. While maintaining the dendritic structure, substituting alkyl chains with OEG chains also considers the following reasons: (1) ethylene glycol can improve the compatibility with LCs,⁵⁴ (2) a more flexible chain could better reshape as an adaptation to the anisotropy change of the environment, and (3) OEG chains enhance the solubility of the ligands and the NPs after ligand exchange, making the system more operational for future applications.

Linear biphenyl alkyl ligand L1 is synthesized as a comparison via a one-pot, two-step procedure (Scheme 1a).

4-Biphenylcarboxylic acid is chlorinated by thionyl chloride and then reacts with alcohol to graft disulfide as the anchoring group on surfaces of precious metal NPs, such as Au. The Fréchet-type dendrimer provides an excellent platform to build on multiple functional moieties. Stynthesis of the branches of dendritic ligands is shown in Scheme 1b, where 4-phenylphenol reacts first with an asymmetrically activated bridging chain, either bromo-undecanol 2 or tosylated OEG 3, then with tosyl chloride and gets attached to methyl gallate via the Williamson etherification to yield 8 or 9. Two synthetic procedures are adopted from the previous works in our group to anchor the dendritic ligands onto NPs of different materials for generalization (Scheme 1c). St. For the thiol-terminated ligands L2 and L3, methylbenzoate 8 or 9 is hydrolyzed under basic conditions, and the resulting benzoic acid 10 or 11

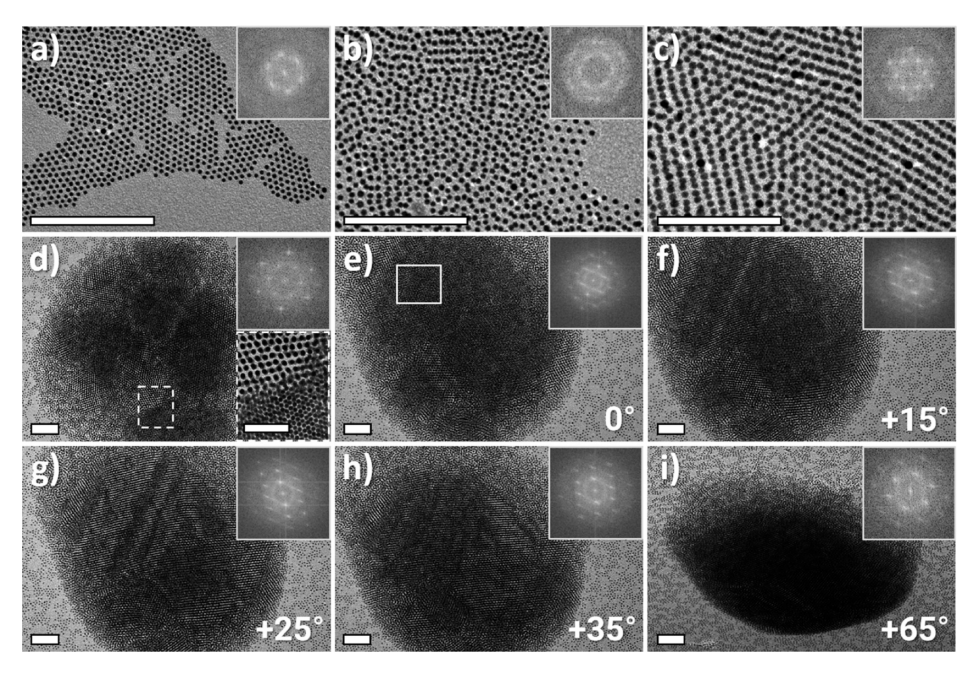


Figure 3. TEM images of Au NPs after ligand exchange with the fast Fourier transform images. (a) Monolayer of Au-L1. A multilayer of (b) Au-L2 and (c) Au-L3. (d) Micron-scale "superball" self-assembly of Au-L3 NPs with multiple superlattice domains. The inset at the bottom right corner is a zoom-in of the circled area. (e-i) Series of tilt angle images of another superball showing the electron channeling effect in the structure. The fast Fourier transform images are transformed from the same position in (e). A tomography video to reconstruct the 3D structure of the superball is included in the Supporting Information. Scale bars: 100 nm and the inset of (d) 50 nm.

follows the same procedure as L1 to give the final thiolated ligands L2 or L3. For the phosphonic acid-functionalized ligands L4 and L5, the benzoates are reduced with LiAlH₄ to yield benzyl alcohols 12 and 13, followed by chlorination into 14 and 15. Benzyl azides 16 and 17 are converted from chlorides, allowing the graft of the anchoring group, phosphonic acid, via the Huisgen "click" cycloaddition. Scheme 2 shows the summary of dendritic promesogenic ligands L2 to L5, while the details of syntheses and characterizations are included in the Supporting Information.

Comparing the POM images of L1, L2, and L3 (Figure 2ac), L1 displays a great tendency to form large crystalline domains with a clear fan-shaped, focal conic pattern. L2 crystallizes into very small domains as the complicated dendritic structure may not favor the formation of large, well-ordered crystal regions like L1. L3 is not birefringent and does not crystallize. Differential scanning calorimetry (DSC) shows L1 and L2 both have a sharp freezing peak, whereas L3 only has a glass transition at around −10 °C. Powder X-ray diffraction (XRD) results further confirm the absence of crystallinity in L3 (Figure S1). Similarly, compared to L4, of which the DSC and XRD results are classic crystalline solids, L5 behaves more like a semicrystalline material (Figures S4 and S5). Therefore, the design of using OEG chains in dendritic promesogenic ligands can significantly promote flexibility and softness of the molecule, which is shown to be of great importance in increasing the miscibility and stability of NPs in the LC matrixes in the following experiments. Details of DSC and XRD at room temperature and elevated temperatures and videos of temperature-dependent POM are included in the Supporting Information.

Ligand Exchange with NPs. The promesogenic ligands are grafted onto NPs through a solvent-mediated ligand exchange process (denoted as NP-L after ligand exchange). For the case of Au NPs, the promesogenic ligand L1, L2, or L3

is dissolved in chloroform (10 mg/mL) and rigorously stirred with Au-Oleyl amine (Olam) NPs in hexanes (10 mg/mL) at room temperature for 1 h. The Au NPs are then precipitated with antisolvents (acetone or isopropanol for L1 and L2, methanol for L3). The sediments are collected after centrifugation and redispersed in chloroform. This purification step is repeated three times to ensure the complete removal of unbound ligands. To demonstrate the generality of the ligand design, two different lengths of CdSe/CdS NRs (NR1 and NR2) and Gd_2O_3 triangular nanoplatelets are also ligand exchanged with L4 and L5. Detailed procedures for NP syntheses, ligand exchange, and ligand grafting density are described in the Materials section and the Supporting Information.

Transmission electron microscopy (TEM) images show that Au NPs after ligand exchange with L1, L2, and L3 can be welldispersed in chloroform and can self-assemble into mono- or multilayer structures (Figure 3a-c). Moreover, Au-L3 reproducibly presents an assembled micron-scale "superball" structure when the NPs are drop-casted onto the TEM grid (Figure S9), which is rarely seen in the case of Au-Olam, L1, or L2 under the same condition. The superball consists of several well-ordered superlattice domains with different orientations, as shown in the inset of a zoom-in image (Figure 3d). The reconstruction of the superball shows the appearance and disappearance of the lines generated from the electron channeling effect as the tilt angle changes (Figure 3e-i). It is hypothesized that, based on the molecular structure and the amphiphilic nature of the L3 ligand, the peripheral biphenyls and the OEG chains are both playing a role during the drying process, where the biphenyl π - π interaction facilitates stacking of the NPs as the solvent evaporates out, and the flexible OEG chains promote the fine adjustment of the NPs to the enthalpically favored positions, forming several ordered superlattice domains.⁵⁷ The polarity difference between the

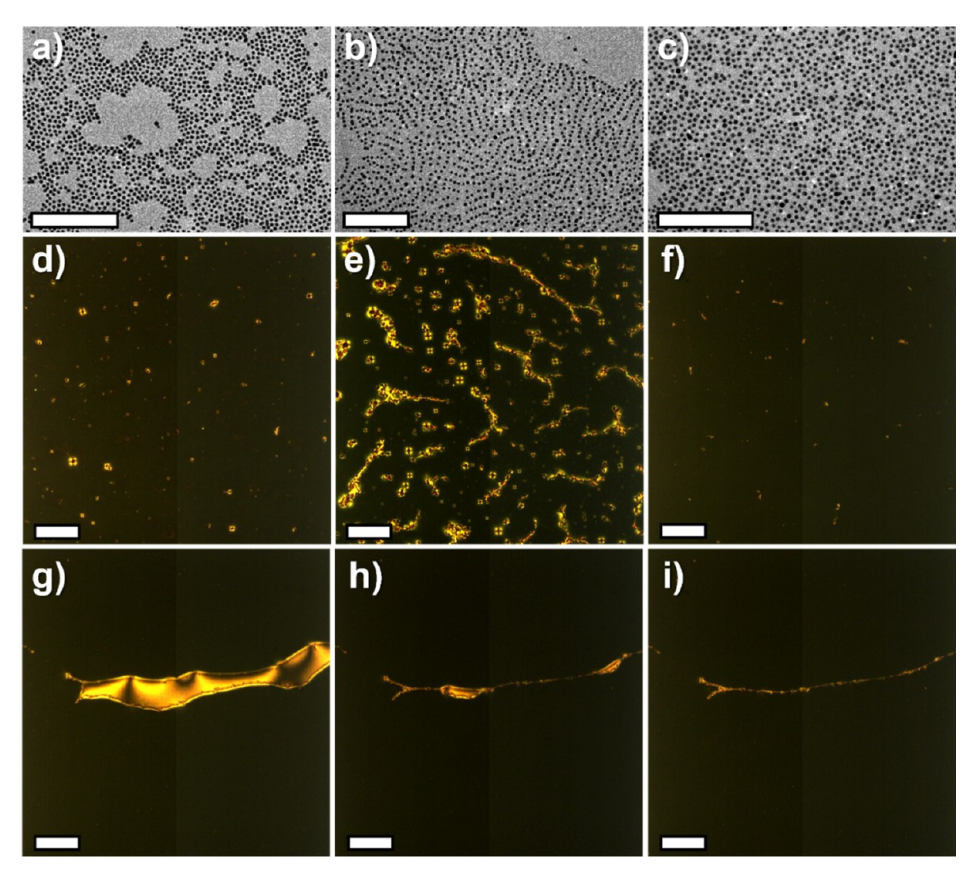


Figure 4. Miscibility of Au-L in nematic 5CB. (a–c) TEM images of Au-L1, L2, and L3 in 5CB. More examples of the "threaded beads" of Au-L2 NPs are shown in Figure S9d–f POM images with 90° crossed polarizers of 1.0 wt % of Au-L1, L2, and L3 in nematic 5CB at 25 °C. (g–i) Dynamic assembly process of Au-L3 NPs during the equilibration of mesogens realigning toward the homeotropic alignment. Scale bars: (a–c) 100 nm and (d–i) 200 μ m.

amphiphilic ligands and the dispersant environment also helps the formation of superballs. Detailed characterizations of the NPs after ligand exchange are included in the Supporting Information.

Miscibility and Dynamics of NP-L in 5CB. After ligand exchange, dispersions of Au-L in 5CB are prepared by sonicating the vacuum-dried Au-L NPs in isotropic 5CB. The mass of dried NPs is weighed out, and a calculated volume of 5CB is added to control the loading ratio of NPs in 5CB. NPs with surface decoration of promesogenic ligands can be dispersed well by being sonicated in isotropic 5CB for about 3 min, resulting in a ruby-red solution. 1.0 wt % (10 mg/mL) of each Au-L in 5CB dispersions is prepared as the stock solutions and further diluted with neat 5CB for optical characterizations. This mixing method is relatively "fast and clean" which precisely controls the concentration of Au-L in 5CB and guarantees no disturbance from any residual solvents like chloroform. NPs without biphenyl decoration can barely be dispersed in isotropic 5CB. Au-Olam or Au-dodecanethiol NPs can only be coarsely suspended into the isotropic phase even with extended sonication time, forming a dark purple mixture, and sediment quickly to the bottom after several minutes (Figure S13).

The TEM images of Au-L NPs dispersed in 5CB show that most of the particles are well-separated for all three ligands (Figure 4a-c). Interestingly, Au-L2 presents large areas with a pattern of "threaded beads" with an interline edge-to-edge distance of 5–7 nm (Figure S10). Considering the size of the L2 ligand (dried, approx. 2 nm) and the 5CB mesogen

(theoretical evaluation approx. 2 nm), this pattern may be generated from the ligand-LC matrix interactions, and there could be one to two layers of 5CB sandwiched in between the promesogenic ligands. 58

With the same loading ratio of 1.0 wt %, all of the Au-L have decent miscibility with 5CB by visual examination, supporting the advantage of using biphenyl-decorated ligands to disperse NPs in cyanobiphenyl-derived LCs. Characterizations with POM are conducted to investigate the distribution of NPs in nematic 5CB. For undoped, equilibrated 5CB POM specimens, the homeotropic alignment perpendicular to the glass substrates results in a structure without birefringence under 90° crossed polarizers. For 5CB doped with NPs, when the miscibility is not ideal and the size of NP aggregates reaches over the De Gennes-Kleman limit (usually 0.1 to 1 μ m for 5CB), 59,60 the anchoring effect at the NP surfaces breaks the local homeotropic alignment, and bright areas show up under POM. Therefore, the miscibility can be represented qualitatively by the area of the bright spots in POM images, where a smaller bright area indicates better miscibility in homeotropic 5CB. Specimens are prepared with pre-warmed Au-L in isotropic 5CB (50 °C) and naturally cooled to room temperature. The POM results show that Au-L1 and Au-L3 both have relatively small bright areas, whereas Au-L2 has some large agglomerates (Figures 4d-f and S14).

A dynamic assembly process of Au-L3 agglomerates driven by the equilibration of the LC matrix is captured (Figure 4g i). Au NPs are trapped at the interface between an equilibrated homeotropic domain and a non-equilibrated nematic domain

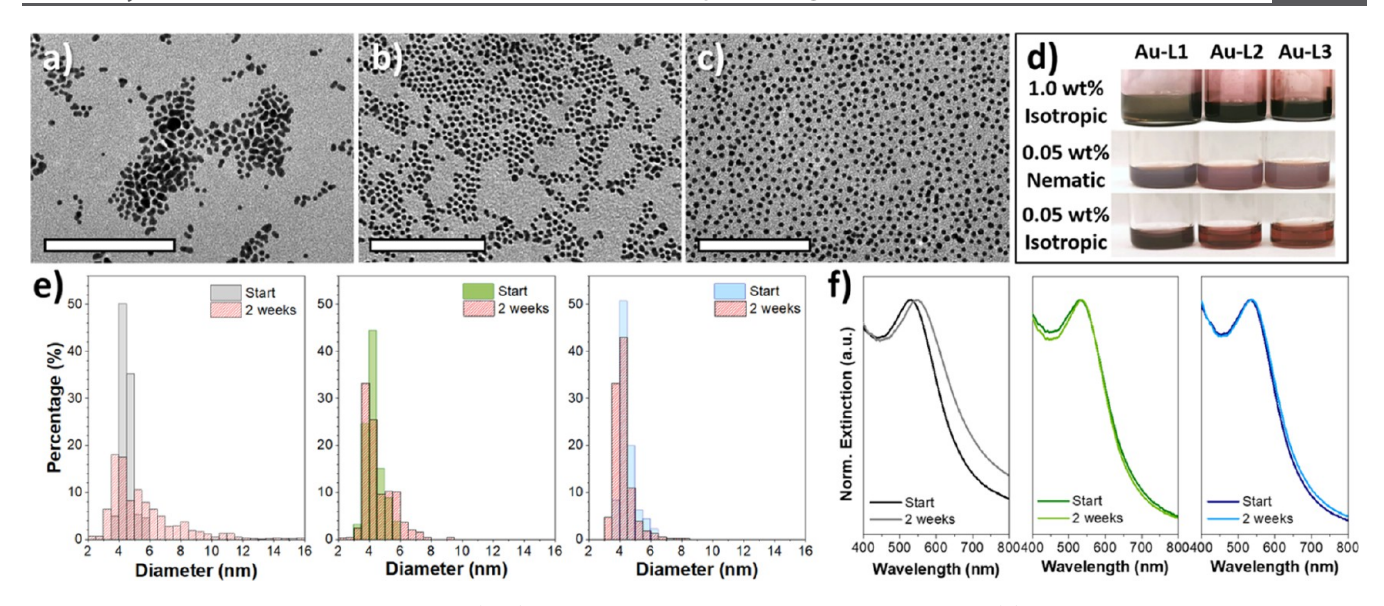


Figure 5. Shelf-life test of Au-L in nematic 5CB. (a-c) TEM images of Au-L1, L2, and L3 after 2 weeks. (d) Photos of samples after 1 month. All samples were sonicated beforehand. (e) Size distribution and (f) optical extinction spectra of Au-L1 (black), Au-L2 (green), and Au-L3 (blue) at the beginning and after 2 weeks measured with diluted Au-L in 5CB (0.05 wt %). Scale bars: (a-c) 100 nm.

to minimize the energy. 30,61-63 As the equilibration proceeds and the non-equilibrated domain shrinks, the Au NP agglomerates move along with the domain boundary. When the whole system is equilibrated, the Au NPs form a characteristic curved line, leaving a footprint of a previous defect (Figures S15d-f and S16). Previously, West et al. reported NP aggregates formed at the interfaces of isotropic and nematic phases could be dragged by the sweeping of the cooling frontier. They also derived the largest particle radius which could be dragged by the interface and should increase as the anchoring coefficient increases.

Here, in our case, the Au-L3 NP agglomerates generated at the interface between two nematic domains with different mesogen alignments get pushed by the movement of the boundary. A similar dynamic process also appears for Au-L2 (Figure S15a-c). However, such a process or the final characteristic curves do not show up in the Au-L1 specimen. It seems reasonable to infer that the dynamic assembly would mostly happen when the dendritic ligands are applied at the surface. Indeed, TGA results of Au-L NPs show that, although the ligand density is the highest for L1, the peripheral biphenyl density of L2 and L3 is two to three times higher than that of L1 (Table S5), which promotes the penetration and interdigitation between 5CB mesogens and the surface ligands and increases the anchoring force to move Au NPs along the domain edges. The transition of the matrix could serve as a new strategy to manipulate the self-assembly of NPs or to build up smart responsive materials.¹¹

It should be noted that the preparation procedure for POM specimens is of great importance. In the nematic phase, the matrix mesogens expel NPs even with the promesogenic ligand coating. When the Au-L NPs in 5CB are not pre-warmed and are loaded in the nematic phase, all three of them still heavily aggregate even after an extended time of sonication (Figure S17). Fast quenching of the specimen from high temperatures to room temperature results in the formation of a disordered system (Figure S20). The confined distance between glass substrates and the cooling rate cannot be ignored in this dynamic process.

While the dynamics of the matrix are actively engaging in the assembly of dopants, influence from the dopants is also altering the properties of the matrix. When 1.0 wt % of Au-L are doped into 5CB and the system is cooled down from the isotropic phase, the original alignment of the mesogens is interrupted, and the transition temperature ($T_{\rm NI}$) decreases compared to neat 5CB: the peak temperature decreases by 0.18 °C for Au-L2, 0.30 °C for Au-L1, and 0.38 °C for Au-L3 (Figure S21a). The DSC trend should result from the miscibility difference. When the NPs are not well-dispersed in 5CB, the influence from the NP dopants to the LC matrix is limited, and mesogens maintain the original alignment in neat 5CB as much as possible.

Stability of NP-L in 5CB. The stability tests are conducted at room temperature and elevated temperatures. 1.0 wt % of Au-L NPs in nematic 5CB is left at 25 °C for the shelf-life test and are characterized qualitatively with visual examination and quantitatively with TEM and UV-vis spectroscopy (Figure 5). After 2 weeks, fused Au-L1 NPs can be found in TEM, and the size distribution has changed from 4.54 \pm 0.36 to 5.55 \pm 2.25 nm. The surface plasmonic resonance peak has shifted for 20.6 nm and has also broadened, representing the presence of fused, polydispersed Au NPs (Table S4). A layer of Au-L1 coating with a golden color, indicating the formation of bulk Au, was found at the bottom of the vial after 1 month, which will not be able to get redispersed into 5CB (Figure S22a). Although L1 can help disperse Au NPs in 5CB, it fails to protect the NPs and maintain stability in the nematic 5CB for an extended time.

As a comparison, for Au-L2 and Au-L3 after 2 weeks, the TEM images still present a relatively uniform shape and a narrow size distribution, showing the advantage of using dendritic ligands to protect the NPs. Compared with the start, their surface plasmonic resonance peaks only shift 2–3 nm and there is no significant broadening. A photo taken after 6 months shows the comparison between Au-L1 and Au-L3, where Au-L1 had fused and coated around the wall of the vial, but Au-L3 was still in good condition (Figure S22b). The cone-shaped molecular structure of dendritic promesogenic

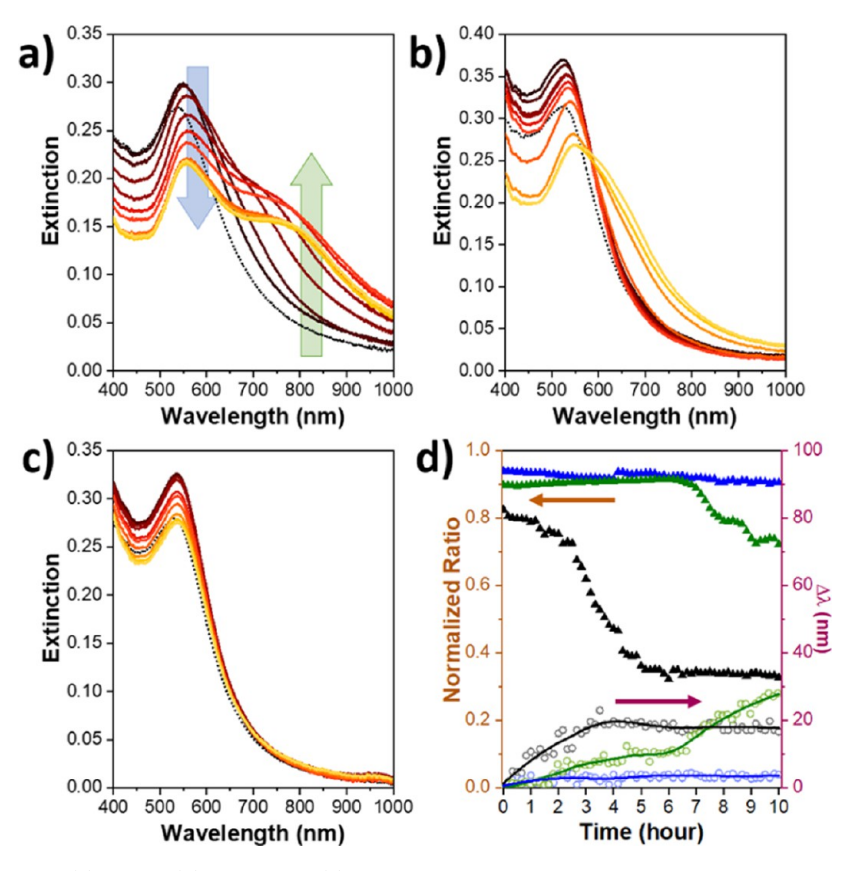


Figure 6. Thermal stability test of (a) Au-L1, (b) Au-L2, and (c) Au-L3 monitored with UV-vis at 50 °C for 10 h. Dashed lines represent the start curve. (d) Summary of the normalized ratio (solid triangles) and the wavelength shift $\Delta\lambda$ (open circles) of Au-L1 (black), Au-L2 (green), and Au-L3 (blue).

ligands confines the degree of freedom of surface ligands and thus helps to preserve NPs.

A good thermal stability of the LC-NP hybrid system guarantees future applications conducted under higher temperatures for a longer time with good reproducibility. As a model system, the stability of Au-L NPs in isotropic 5CB is qualitatively measured at 35 and 50 °C with visual examination and quantitatively monitored at 50 °C with UV—vis spectroscopy. Tables S6 and S7 show that at 35 °C, it takes 12, 48 h, and more than 6 days for Au-L1, Au-L2, and Au-L3, respectively, to display visible changes from ruby-red dispersions to purple/blue precipitates. The extinction spectra of Au-L3 stored in a 35 °C water bath over 6 days further support the conclusion (Figure S24).

To closely monitor the changes, 0.05 wt % of Au-L NPs in 5CB is heated up to 50 °C and continuously characterized with UV-vis every 10 min for 10 h. For clarity, Figure 6a-c gives a portion of the results, where the start curves are plotted with dotted lines, and the color gradient from black to yellow represents the curve of every hour. The extinction intensities of all samples have a trend of "increase then decrease". The increase in extinction during the first hour is caused mainly by the ramping of temperatures. The start curves are collected at the moment when the mixture in the cuvette transforms from the nematic to the isotropic phase, which means the actual temperature has not reached 50 °C. As the temperature ramps up, the peak intensity of the curve increases during the first hour due to the decrease of the refractive index of 5CB.⁶⁹ The full data set shows that this equilibrating process usually takes around 1 h (Figure S25a-c). After the first hour, the overall

intensity decreases gradually, which may result from the slow precipitation of the Au NPs to the bottom of the cuvette.

Due to the fusing of NPs under a high-temperature environment, the optical extinction peak red-shifts and broadens up, accompanied by an increase of intensity in the long-wavelength region. This is quantitatively represented by two indices: the normalized ratio and the peak wavelength shift $(\Delta \lambda)$. In the plot of Au-L1, a shoulder peak at 800 nm gradually appears (Figure 6a). Considering that the overall intensity evolves with time, and the initial concentration of different samples are slightly different, the normalized ratio between small NPs and large fused NPs is calculated as follows

normalized ratio =
$$\frac{\text{intensity (peak)} - \text{intensity (800 nm)}}{\text{intensity (peak)}}$$

Figure 6d includes both indices. For Au-L1, the ratio starts with a relatively slow decrease, indicating a reduction of the portion of small NPs, followed by a dramatic drop from the second to the fifth hour, then remains almost unchanged until the measurement ends. Meanwhile, the red shifts keep increasing in the first 3 h and then reach a plateau of 20 nm. Both dendritic ligands can delay the decrease of the normalized ratio and slow down the speed of shifting. Moreover, compared with Au-L2, which shows a turning point after 7 h, it is remarkable that the normalized ratio of Au-L3 almost does not change during this 10 h test other than a slight decrease in the overall intensity. The peak shift is only 5 nm compared to the start.

It is worth noticing that using aged samples will result in bad thermal stability (Figure S25d-f). After being stored on the

shelf for 1 week, Au-L1 decays quickly during the first 10 min, accompanied by a significant increase of the peak intensity at 800 nm. Au-L2 can maintain good shape for about 3 h. Au-L3 broadens and red-shifts for 50 nm in the first hour, but it remains almost unchanged during the following test. Therefore, although all of the 1.0 wt % Au-L NPs in 5CB give less stability time than their corresponding freshly prepared samples, both dendritic ligands still show better performance than the linear ligand, providing much convenience and decent reproducibility for potential characterizations.

Proposed Ligand Arrangement. Previous research proposed the reshaping and reordering of linear ligands around the NPs in nematic LC. In an anisotropic LC matrix, the ligand corona cannot maintain isotropic as in traditional solvents: the axial ligands elongate and the equatorial ligands shrink; ligands may also migrate from the equatorial plane to the axial poles. Based on this, the POM results in Figure 4 can be explained by the proposed ligand configuration at the surface of NPs in nematic 5CB (Figure 7). Among these three

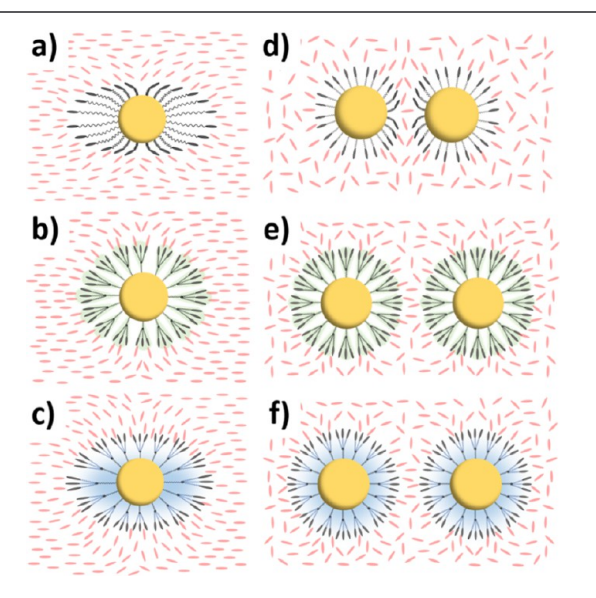


Figure 7. Illustration of the proposed ligand arrangement. In nematic 5CB: (a) Au-L1, (b) Au-L2, and (c) Au-L3. In isotropic 5CB: (d) Au-L1, (e) Au-L2, and (f) Au-L3.

ligands, L1 with a linear configuration should have the smallest steric hindrance to deform and migrate. The dendritic structure yields compact molecules with less deformability and limited mobility, 53 which could retard the reshaping and repositioning process of L2 and thus result in the most NP agglomerations. However, although the mobility of L3 is also confined by the dendritic structure, with the help of flexible OEG chains, L3 could still reshape and deform promptly as a response to the anisotropic environment, giving excellent performance in the miscibility study.

During the shelf-life test at room temperature, it is the limited mobility of both dendritic ligands that makes the equatorial planes of Au-L2 and L3 less exposed in nematic 5CB compared to that of Au-L1. The highly organized ligand capping helps prevent Au NPs from fusing and leads to longer shelf-life time in this case.

In the isotropic phase, the anisotropic supramolecular alignment of mesogens is lost. The ligand arrangement on a spherical NP switches back to a more common case: a uniform corona. However, for NPs covered with linear promesogenic ligands, when two particles are approaching each other, deformation of the linear ligands leads to a failed formation of a well-ordered protection layer (Figure 7d), which will eventually cause faster fusing and precipitating. On the contrary, the packing of branches of dendritic ligands is better confined by the molecular structure. Both dendrimers maintain the original capping when NPs are getting closer and elongate the lifetime of Au under heating (Figure 7e,f).

Generalization of the Design. The ligand design can also be generalized to a wider range of NPs by switching the binding groups, which allows the potential of adding more functionalities to the LC-NP hybrid systems. The organic synthesis procedure is highly modulated. Figure 8 gives examples of some anisotropic NPs 1.0 wt % in 5CB, such as fluorescent NRs with different dimensions and Gd₂O₃ triangular nanoplatelets which can be further doped to form nanophosphors. In general, large NPs are less miscible than small Au NPs, but the agglomerates are still uniformly distributed. Although NR1 and NR2 are both rods, the final POM patterns are still different even with the same ligand (Figure 8d,e). For example, NR1-L4 forms connected networks, whereas NR2-L4 forms irregularly shaped islands. Gd₂O₃ nanoplatelets have a high propensity for bundle

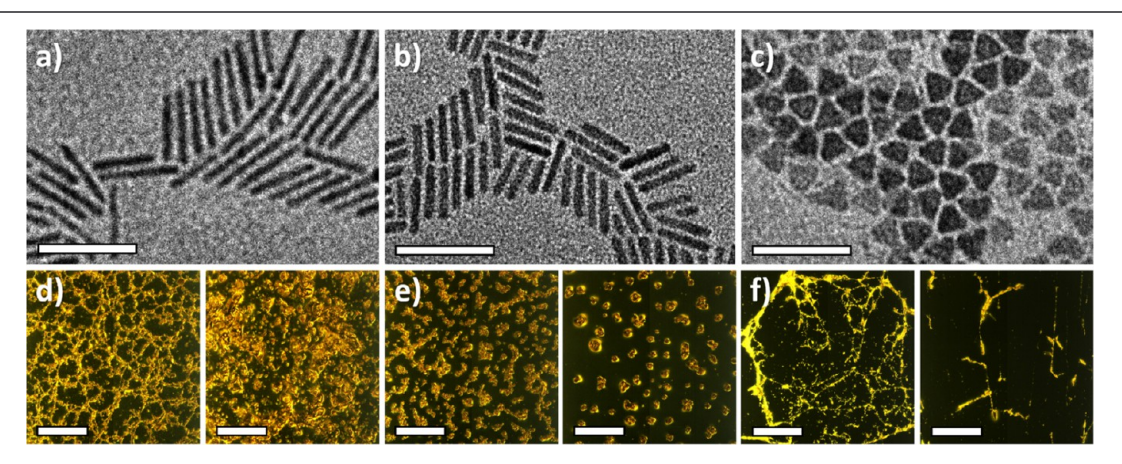


Figure 8. TEM images of as-synthesized (a) NR1, 39.1 nm \times 3.1 nm, (b) NR2, 28.1 nm \times 4.3 nm, and (c) Gd₂O₃, edge length 14.9 nm and thickness 2.1 nm. POM images of (d) NR1, (e) NR2, and (f) Gd₂O₃. NP-L4 on the left and NP-L5 on the right. Specimens pre-warmed. Scale bars: (a-c) 50 nm and (d-f) 100 μ m.

formation (Figure S12), which generates long bright fibers under POM (Figure 8f). The results indicate that the assembly nature of NPs can play an important role in the LC-NP hybrid systems. The list should not be limited to the abovementioned examples. A video of NR2-L4 showing the formation of POM patterns is included in the Supporting Information.

CONCLUSIONS

In summary, we designed and synthesized two types of promesogenic ligands with the dendritic structure and compared their capability of stabilizing of NPs in LCs with the linear ligands. We showed that the cone shape of the dendritic ligands facilitates the formation of a compact organic capping layer to keep NPs separated and enhances the stability of NPs in nematic and isotropic 5CB. While maintaining the dendritic structure, substituting the alkyl chains with the OEG chains promotes the response of the ligand shell to the external anisotropic environment, which eventually leads to good miscibility and stability at the same time. Bridged by dendritic promesogenic ligands, a dynamic assembly process of Au agglomerates along the defect boundaries driven by the equilibration of 5CB mesogens toward the homeotropic alignment is captured. NPs of other materials with anisotropic shapes capped by dendritic promesogenic ligands are also dispersed in the LC matrix uniformly, showing the generality of such a design. With this systematic study on the "LCpromesogenic ligand-NP" hybrid system, we hope to pave the way for implementing versatile NPs into the LC matrix with great stability and stimulate the research of NP self-assembly behavior in a dynamic, stimuli-responsive environment.

EXPERIMENTAL SECTION

Materials. 4'-Pentyl-[1,1'-biphenyl]-4-carbonitrile (98%) was purchased from Ambeed. Thionyl chloride (>98%), 11-bromo-1undecanol (>97%), and lithium aluminum hydride (>95%) were purchased from TCI. 4-Biphenylcarboxylic acid (99%), methyl 3,4,5trihydroxybenzoate (99%), and sodium azide (99%) were purchased from Acros Organics. 4-Phenylphenol (97%), triethylene glycol (99%), and 4-(dimethylamino) pyridine (≥99%) were purchased from Aldrich. (+)-sodium L-ascorbate (≥99%) was purchased from Sigma. 11-Mercapto-1-undecanol (97%), 4-toluenesulfonyl chloride $(\geq 98\%)$, potassium iodide (99%), and 1-dodecanethiol $(\geq 98\%)$ were purchased from Sigma-Aldrich. Triethyl amine (99%) was purchased from Alfa Aesar. 10-Undecynylphosphonic acid (≥97%) was purchased from SiKÉMIA. Copper(II) sulfate pentahydrate, potassium hydroxide (ACS reagent), anhydrous potassium carbonate (ACS reagent), and anhydrous sodium sulfate were purchased from Fisher Scientific. All chemicals were used as received. Silica gel (P60, 230-400 mesh) was purchased from SiliCycle. Anhydrous dichloromethane (99.8%, extra dry over molecular sieves) was purchased from Acros Organics. Acetone, ethanol, methanol, isopropanol, chloroform, dichloromethane, hexanes, ethyl acetate, dimethylformamide, and tetrahydrofuran were purchased from Fisher Scientific. All solvents were of ACS grade or higher and were used without further purification.

The borane *tert*-butylamine complex (97%) was purchased from Aldrich. 1,2,3,4-Tetrahydronaphthalene (tetralin, anhydrous, 99%), tetrachloroauric(III) acid trihydrate (99%), oleic acid (technical grade, 90%), oleylamine (technical grade, 70%), 1-octadecene (technical grade, 90%), trioctylphosphine oxide (TOPO, 99%), trioctylphosphine (TOP, 97%), sulfur (99%), selenium (99,99%), and lithium hydroxide monohydrate (99.95%) were purchased from Sigma-Aldrich. Hexadecylamine (HAD, 98%) and octadecylphosphonic acid (ODPA, 99%) were purchased from TCI. Gadolinium acetate (99%) was purchased from GFS chemical. Cadmium oxide

(CdO, 99.5%) and 1-octadecene (ODE, 90%) were purchased from Acros. All chemicals were used as received.

Synthesis of Au NPs. The Au NPs were synthesized according to a reported method. 71,72 200 mg of $HAuCl_4\cdot 3H_2O$ was dissolved with $10\,$ mL of tetralin and $10\,$ mL of Olam in a three-neck flask with stirring and N_2 flow. 90 mg of borane tert-butylamine was dissolved with $1\,$ mL of tetralin and $1\,$ mL of Olam and the solution was injected swiftly into the flask. The mixture turned deep red upon injection and was stirred at room temperature for $3\,$ h with continuous N_2 flow. Au NPs were collected by precipitating with 80 mL of acetone and centrifuging at 8000 rpm for 3 min. The sediment was redispersed into $10\,$ mL of hexanes, precipitated with 80 mL of ethanol, and centrifuged at 8000 rpm for 3 min twice. The Au NPs were stored in $10\,$ mL of hexanes (approx. $10\,$ mg/mL) for future use.

Synthesis of CdSe/CdS Core—shell NRs. The synthesis of CdSe/CdS NRs follows the seeded growth method of Carbone et al., which requires synthesizing CdSe cores through hot injection at 380 °C and rapid cooling as the first step. To grow the CdS shell, a mixture of 60 mg of CdO, 3 g of TOPO, and 290 mg of ODPA are charged in a three-neck flask. After the flask is vacuumed for an hour at 150 °C, the solution is heated to 350 °C under nitrogen. 1.5 g of TOP is injected and the temperature is allowed to return to 350 °C. The solution of 3 mg CdSe cores is injected with an S-TOP solution (120 mg of S in 1.2 mL of TOP). The nanocrystals are left to grow for 10 min before being rapidly cooled with an air gun. The particles are purified twice with ethanol and redispersed in hexanes. 73,74

Synthesis of Gd_2O_3 NPs. The synthesis method was adopted from a previous publication. The synthesis method was added into a mixture of 9 mL of oleic acid, 6 mL of Olam, and 15 mL of 1-octadecene and was heated to 130 °C under vacuum for 1 h to remove H_2O . After 2.0 mmol of gadolinium acetate was added, the solution was evacuated at the same temperature for another hour. The reaction solution was then heated to 320 °C for 1 h under N_2 , yielding the Gd_2O_3 triangular nanoplates. At 150 °C, the reaction solution was quenched to room temperature through the addition of toluene. Purification is conducted by adding excess methanol and centrifuging at 6000 rpm for 5 min.

Ligand Exchange Procedure. Ligand exchange of Au NPs with promesogenic ligands was done at room temperature for 1 h with vigorous stirring. 10 mg of promesogenic ligands (**L1**, **L2**, or **L3**) was dissolved with 1 mL of chloroform, followed by adding 1 mL of 10 mg/mL Au NP solution in hexanes. Au-**L1** NPs were collected by precipitating the mixture with 12 mL of isopropanol and centrifuging at 8000 rpm for 3 min, then redispersed with 2 mL of chloroform. This procedure was conducted three times to remove excess free ligands. Au-**L2** NPs were precipitated with acetone for the first cycle and isopropanol for the following two cycles. Au-**L3** NPs were precipitated with methanol three times.

Ligand exchange of NRs and Gd_2O_3 NPs with L4 and L5 was performed with stirring at 50 °C overnight. Precipitation with isopropanol for NP-L4 or hexanes for NP-L5 was conducted three times to purify the NPs. After ligand exchange, all NPs (Au, NRs, and Gd_2O_3) were stored in 2 mL chloroform for future use (approx. 5 mg/mL).

Preparation of NPs in 5CB. Vacuum-dried Au-L NPs were weighed out to measure the accurate mass. A calculated amount of 5CB was added to the vial to prepare the 1.0 wt % of Au-L 5CB dispersion. The mixture was sonicated at 40 °C for 3 min, forming a uniform deep red solution. The 0.05 wt % of Au-L in 5CB was prepared by diluting the corresponding 1.0 wt % samples with neat 5CB. Gd₂O₃-L in 5CB samples were prepared with the same procedure, where the final mixtures were transparent in the isotropic phase and opaque white in the nematic phase. All NP-L in 5CB was stored at room temperature and well-sonicated before any characterization

Preparation of POM Specimens. 1.0 wt % of all NP-L in 5CB samples was heated to the isotropic phase on top of a hot plate set at 50 $^{\circ}$ C. The mixtures were added into the gap between two glass substrates (also heated on the hot plate) with a fixed distance of 60 μ m and naturally cooled to room temperature for POM character-

ization. All samples and glass substrates were pre-warmed at the same temperature for a long enough time and cooled without any other facilities or operations.

Preparation of TEM Specimens. NPs in 5CB were drop-casted on the TEM grids and allowed to settle for 1 h. Then, the grid was held by tweezers and dipped into a solvent (methanol or acetone for L1, L2, and L4; hexanes for L3 and L5) several times to wash off 5CB. The specimens were then dried in vacuo to remove solvent residues.

Nuclear Magnetic Resonance Spectroscopy. 1 H NMR (400 MHz) and 13 C NMR (101 MHz) spectra were recorded on Bruker Avance NEO400 NMR spectrometer. 1 H and 13 C chemical shifts (δ) are reported in ppm, while coupling constants (J) are reported in Hertz (Hz). The multiplicity of signals in 1 H NMR spectra is described as "s" (singlet), "d" (doublet), "t" (triplet), "q" (quartet), "p" (pentet), "dt" (doublet of triplets), "td" (triplet of doublets), and "m" (multiplet). All spectra were referenced using solvent residual signals (CDCl $_3$: 1 H, δ 7.26 ppm; 13 C, δ 77.16 ppm, labeled in red). Other solvent residual peaks were labeled in gray. Compounds were purified by filtration, precipitation, crystallization, or column chromatography, as indicated in corresponding procedures.

Mass Spectroscopy. Matrix-assisted laser desorption ionization time-of-flight (MALDI-TOF) mass spectrometry was performed on a Bruker rapifleX (MALDI-TOF/TOF) mass spectrometer using dithranol as the matrix.

Thermal Analysis. Thermal transitions were determined on a TA Instruments Q2500 differential scanning calorimeter equipped with a liquid nitrogen cooling system. Ligand grafting density was measured with a PerkinElmer Diamond thermogravimetric/differential thermal analyzer under argon from 50 to 500 $^{\circ}\text{C}$ with a heating rate of 20 $^{\circ}\text{C}/\text{min}$

X-ray Diffraction. Powder XRD of neat ligands was performed on Rigaku SmartLab. Measurements at room temperature were collected in the 2θ range of $10.0-60.0^{\circ}$ using a Rigaku SmartLab high-resolution diffractometer with Cu K α radiation (λ = 0.15416 nm, 55 mA and 40 kV) at a resolution of $0.04^{\circ}/2\theta$ and a scan speed of $1.0^{\circ}/2\theta$ min. Temperature-dependent measurements were done with an Anton Paar DHS 1100 Domed Hot Stage at a scan speed of $2.0^{\circ}/min$.

Transmission Electron Microscopy. TEM micrographs were collected using a JEOL 1400 microscope operated at 120 kV equipped with a Gatan Orius 832 camera. TEM was calibrated using a MAG*I*CAL TEM calibration standard.

Polarized Optical Microscopy. The samples of 5CB doped with NPs were observed under crossed polarizers using a Zeiss Axiovert 200 M inverted microscope with a CCD camera accessory connected to a computer.

Optical Extinction Spectroscopy. Optical extinction spectra were collected using a Cary 5000 UV—vis—NIR spectrophotometer for NPs dispersed in chloroform. Temperature-elevated UV—vis spectra were conducted on an Ocean Optics Flame and were set to be collected automatically every 10 min for the thermal stability tests.

Dynamic Light Scattering. Sizes of Au-L NPs dispersed in chloroform (25 °C) were measured with a Malvern Zetasizer in the 173° backscatter mode.

ASSOCIATED CONTENT

Supporting Information

The Supporting Information is available free of charge at https://pubs.acs.org/doi/10.1021/acs.chemmater.3c00057.

Characterizations of neat ligands; additional data of NP-L; miscibility of NP-L in 5CB; stability of NP-L in 5CB; synthesis of promesogenic ligands; and copies of ¹H and ¹³C NMR spectra (PDF)

Temperature-dependent POM of neat ligand L1 (MP4) Temperature-dependent POM of neat ligand L2 (MP4) Tomography video of the Au-L3 superball (MP4) POM of the natural cooling process of NR2-L4 1.0 wt % in 5CB (MP4)

AUTHOR INFORMATION

Corresponding Author

Christopher B. Murray — Department of Chemistry, University of Pennsylvania, Philadelphia, Pennsylvania 19104, United States; Department of Materials Science and Engineering, University of Pennsylvania, Philadelphia, Pennsylvania 19104, United States; Email: cbmurray@sas.upenn.edu

Authors

Yifan Ning — Department of Chemistry, University of Pennsylvania, Philadelphia, Pennsylvania 19104, United States; Occid.org/0000-0001-8033-0904

Zhe Liu — Department of Chemical and Biomolecular Engineering, University of Pennsylvania, Philadelphia, Pennsylvania 19104, United States

Shengsong Yang – Department of Chemistry, University of Pennsylvania, Philadelphia, Pennsylvania 19104, United States

Yuma Morimitsu — Department of Chemical and Biomolecular Engineering, University of Pennsylvania, Philadelphia, Pennsylvania 19104, United States

Chinedum O. Osuji — Department of Chemical and Biomolecular Engineering, University of Pennsylvania, Philadelphia, Pennsylvania 19104, United States; orcid.org/0000-0003-0261-3065

Complete contact information is available at: https://pubs.acs.org/10.1021/acs.chemmater.3c00057

Author Contributions

The manuscript was written through the contributions of all authors listed. All authors have given approval for the final version of the manuscript.

Notes

The authors declare no competing financial interest.

ACKNOWLEDGMENTS

The authors acknowledge the support from the National Science Foundation (NSF) through the Materials Research Science and Engineering Center at the University of Pennsylvania (DMR-1720530). S.Y. acknowledges the support from the National Science Foundation under grant no. DMR-2019444 (IMOD an NSF-STC). C.B.M. also acknowledges the Richard Perry University Professorship at the University of Pennsylvania. C.O. also acknowledges additional support from NSF under grant no. DMR-1945966. This research used resources from the Center for Functional Nanomaterials (CFN) supported by the U.S. DOE Office of Science Facilities at Brookhaven National Laboratory (BNL) under contract no. DE-SC0012704. We thank Dr. D. Nykypanchuk, Dr. G. Doerk, Dr. S. Cetindag, and Dr. F. Lu from BNL-CFN for their help and support.

REFERENCES

- (1) Schadt, M.; Seiberle, H.; Schuster, A. Optical Patterning of Multi-Domain Liquid-Crystal Displays with Wide Viewing Angles. *Nature* **1996**, *381*, 212–215.
- (2) Beeckman, J. Liquid-Crystal Photonic Applications. Opt. Eng. 2011, 50, 081202.
- (3) Kim, D. S.; Lee, Y.-J.; Wang, Y.; Park, J.; Winey, K. I.; Yang, S. Self-Folding Liquid Crystal Network Filaments Patterned with Vertically Aligned Mesogens. ACS Appl. Mater. Interfaces 2022, 14, 50171.

- (4) Liu, M.; Jin, L.; Yang, S.; Wang, Y.; Murray, C. B.; Yang, S. Shape Morphing Directed by Spatially Encoded, Dually Responsive Liquid Crystalline Elastomer Micro-actuators. *Adv. Mater.* **2022**, *35*, 2208613.
- (5) Lee, C.; Ndaya, D.; Bosire, R.; Kim, N. K.; Kasi, R. M.; Osuji, C. O. Fast Photoswitchable Order—Disorder Transitions in Liquid-Crystalline Block Co-Oligomers. *J. Am. Chem. Soc.* **2022**, *144*, 390–399.
- (6) Stamatoiu, O.; Mirzaei, J.; Feng, X.; Hegmann, T. Nanoparticles in Liquid Crystals and Liquid Crystalline Nanoparticles. In *Liquid Crystals*; Tschierske, C., Ed.; *Topics in Current Chemistry*; Springer Berlin Heidelberg: Berlin, Heidelberg, 2011; Vol. 318, pp 331–393.
- (7) Hegmann, T.; Qi, H.; Marx, V. M. Nanoparticles in Liquid Crystals: Synthesis, Self-Assembly, Defect Formation and Potential Applications. J. Inorg. Organomet. Polym. Mater. 2007, 17, 483–508.
- (8) Choudhary, A.; Singh, G.; Biradar, A. M. Advances in Gold Nanoparticle-Liquid Crystal Composites. *Nanoscale* **2014**, *6*, 7743–7756.
- (9) Prakash, J.; Khan, S.; Chauhan, S.; Biradar, A. M. Metal Oxide-Nanoparticles and Liquid Crystal Composites: A Review of Recent Progress. *J. Mol. Liq.* **2020**, *297*, 112052.
- (10) Chen, H.; He, J.; Wu, S.-T. Recent Advances on Quantum-Dot-Enhanced Liquid-Crystal Displays. *IEEE J. Sel. Top. Quantum Electron.* **2017**, 23, 1–11.
- (11) Rodarte, A. L.; Pandolfi, R. J.; Ghosh, S.; Hirst, L. S. Quantum Dot/Liquid Crystal Composite Materials: Self-Assembly Driven by Liquid Crystal Phase Transition Templating. *J. Mater. Chem. C* **2013**, 1, 5527.
- (12) Vardanyan, K. K.; Bates, B. Dielectric and Material Properties of 5CB Nematic Dispersed with Graphene Nanoparticles. *Liq. Cryst.* **2022**, *49*, 264–276.
- (13) Qi, H.; Kinkead, B.; Hegmann, T. Unprecedented Dual Alignment Mode and Freedericksz Transition in Planar Nematic Liquid Crystal Cells Doped with Gold Nanoclusters. *Adv. Funct. Mater.* **2008**, *18*, 212–221.
- (14) Li, W.; Zhu, M.; Ding, X.; Li, B.; Huang, W.; Cao, H.; Yang, Z.; Yang, H. Studies on Electro-Optical Properties of Polymer Matrix/LC/SiO ₂ Nanoparticles Composites. *J. Appl. Polym. Sci.* **2009**, *111*, 1449–1453.
- (15) Agrahari, K.; Vimal, T.; Rastogi, A.; Pandey, K. K.; Gupta, S.; Kurp, K.; Manohar, R. Ferroelectric Liquid Crystal Mixture Dispersed with Tin Oxide Nanoparticles: Study of Morphology, Thermal, Dielectric and Optical Properties. *Mater. Chem. Phys.* **2019**, 237, 121851.
- (16) Demortière, A.; Buathong, S.; Pichon, B. P.; Panissod, P.; Guillon, D.; Bégin-Colin, S.; Donnio, B. Nematic-like Organization of Magnetic Mesogen-Hybridized Nanoparticles: Nematic-like Organization of Magnetic Mesogen-Hybridized Nanoparticles. *Small* **2010**, *6*, 1341–1346.
- (17) Poryvai, A.; Šmahel, M.; Švecová, M.; Nemati, A.; Shadpour, S.; Ulbrich, P.; Ogolla, T.; Liu, J.; Novotná, V.; Veverka, M.; Vejpravová, J.; Hegmann, T.; Kohout, M. Chiral, Magnetic, and Photosensitive Liquid Crystalline Nanocomposites Based on Multifunctional Nanoparticles and Achiral Liquid Crystals. ACS Nano 2022, 16, 11833—11841
- (18) Kubo, S.; Taguchi, R.; Hadano, S.; Narita, M.; Watanabe, O.; Iyoda, T.; Nakagawa, M. Surface-Assisted Unidirectional Orientation of ZnO Nanorods Hybridized with Nematic Liquid Crystals. *ACS Appl. Mater. Interfaces* **2014**, *6*, 811–818.
- (19) Dintinger, J.; Tang, B.-J.; Zeng, X.; Liu, F.; Kienzler, T.; Mehl, G. H.; Ungar, G.; Rockstuhl, C.; Scharf, T. A Self-Organized Anisotropic Liquid-Crystal Plasmonic Metamaterial. *Adv. Mater.* **2013**, *25*, 1999–2004.
- (20) Zeng, X.; Liu, F.; Fowler, A. G.; Ungar, G.; Cseh, L.; Mehl, G. H.; Macdonald, J. E. 3D Ordered Gold Strings by Coating Nanoparticles with Mesogens. *Adv. Mater.* **2009**, *21*, 1746–1750.
- (21) Wang, Y.; Dang, A.; Zhang, Z.; Yin, R.; Gao, Y.; Feng, L.; Yang, S. Repeatable and Reprogrammable Shape Morphing from Photo-

- responsive Gold Nanorod/Liquid Crystal Elastomers. Adv. Mater. 2020, 32, 2004270.
- (22) Jedrych, A.; Pawlak, M.; Gorecka, E.; Lewandowski, W.; Wojcik, M. M. Light-Responsive Supramolecular Nanotubes-Based Chiral Plasmonic Assemblies. *ACS Nano* **2023**, *17*, 5548–5560.
- (23) Nealon, G. L.; Greget, R.; Dominguez, C.; Nagy, Z. T.; Guillon, D.; Gallani, J.-L.; Donnio, B. Liquid-Crystalline Nanoparticles: Hybrid Design and Mesophase Structures. *Beilstein J. Org. Chem.* **2012**, *8*, 349–370.
- (24) Milette, J.; Toader, V.; Reven, L.; Lennox, R. B. Tuning the Miscibility of Gold Nanoparticles Dispersed in Liquid Crystals via the Thiol-for-DMAP Reaction. *J. Mater. Chem.* **2011**, *21*, 9043.
- (25) Qi, H.; Kinkead, B.; Marx, V. M.; Zhang, H. R.; Hegmann, T. Miscibility and Alignment Effects of Mixed Monolayer Cyanobiphenyl Liquid-Crystal-Capped Gold Nanoparticles in Nematic Cyanobiphenyl Liquid Crystal Hosts. *ChemPhysChem* **2009**, *10*, 1211–1218.
- (26) Draper, M.; Saez, I. M.; Cowling, S. J.; Gai, P.; Heinrich, B.; Donnio, B.; Guillon, D.; Goodby, J. W. Self-Assembly and Shape Morphology of Liquid Crystalline Gold Metamaterials. *Adv. Funct. Mater.* **2011**, 21, 1260–1278.
- (27) Kanayama, N.; Tsutsumi, O.; Kanazawa, A.; Ikeda, T. Distinct Thermodynamic Behaviour of a Mesomorphic Gold Nanoparticle Covered with a Liquid-Crystalline Compound. *Chem. Commun.* **2001**, 2640–2641.
- (28) Kanie, K.; Sugimoto, T. Organic—Inorganic Hybrid Liquid Crystals: Hybridization of Calamitic Liquid-Crystalline Amines with Monodispersed Anisotropic TiO ₂ Nanoparticles. *J. Am. Chem. Soc.* **2003**, *125*, 10518–10519.
- (29) Lewandowski, W.; Jatczak, K.; Pociecha, D.; Mieczkowski, J. Control of Gold Nanoparticle Superlattice Properties via Mesogenic Ligand Architecture. *Langmuir* **2013**, *29*, 3404–3410.
- (30) Milette, J.; Cowling, S. J.; Toader, V.; Lavigne, C.; Saez, I. M.; Bruce Lennox, R.; Goodby, J. W.; Reven, L. Reversible Long Range Network Formation in Gold Nanoparticle Nematic Liquid Crystal Composites. *Soft Matter* **2012**, *8*, 173–179.
- (31) Khatua, S.; Manna, P.; Chang, W.-S.; Tcherniak, A.; Friedlander, E.; Zubarev, E. R.; Link, S. Plasmonic Nanoparticles—Liquid Crystal Composites. *J. Phys. Chem. C* **2010**, *114*, 7251–7257.
- (32) Elbert, K. C.; Lee, J. D.; Wu, Y.; Murray, C. B. Improved Chemical and Colloidal Stability of Gold Nanoparticles through Dendron Capping. *Langmuir* **2018**, *34*, 13333–13338.
- (33) Prodanov, M. F.; Pogorelova, N. V.; Kryshtal, A. P.; Klymchenko, A. S.; Mely, Y.; Semynozhenko, V. P.; Krivoshey, A. I.; Reznikov, Y. A.; Yarmolenko, S. N.; Goodby, J. W.; Vashchenko, V. V. Thermodynamically Stable Dispersions of Quantum Dots in a Nematic Liquid Crystal. *Langmuir* **2013**, *29*, 9301–9309.
- (34) Prodanov, M. F.; Buluy, O. G.; Popova, E. V.; Gamzaeva, S. A.; Reznikov, Y. O.; Vashchenko, V. V. Magnetic Actuation of a Thermodynamically Stable Colloid of Ferromagnetic Nanoparticles in a Liquid Crystal. *Soft Matter* **2016**, *12*, 6601–6609.
- (35) Percec, V.; Cho, W.-D.; Ungar, G.; Yeardley, D. J. P. Synthesis and Structural Analysis of Two Constitutional Isomeric Libraries of AB ₂ -Based Monodendrons and Supramolecular Dendrimers. *J. Am. Chem. Soc.* **2001**, *123*, 1302–1315.
- (36) Jishkariani, D.; Elbert, K. C.; Wu, Y.; Lee, J. D.; Hermes, M.; Wang, D.; van Blaaderen, A.; Murray, C. B. Nanocrystal Core Size and Shape Substitutional Doping and Underlying Crystalline Order in Nanocrystal Superlattices. *ACS Nano* **2019**, *13*, 5712–5719.
- (37) Jishkariani, D.; Wu, Y.; Wang, D.; Liu, Y.; van Blaaderen, A.; Murray, C. B. Preparation and Self-Assembly of Dendronized Janus Fe $_3$ O $_4$ –Pt and Fe $_3$ O $_4$ –Au Heterodimers. ACS Nano 2017, 11, 7958–7966.
- (38) Diroll, B. T.; Jishkariani, D.; Cargnello, M.; Murray, C. B.; Donnio, B. Polycatenar Ligand Control of the Synthesis and Self-Assembly of Colloidal Nanocrystals. *J. Am. Chem. Soc.* **2016**, *138*, 10508–10515.

- (39) Elbert, K. C.; Vo, T.; Oh, D.; Bharti, H.; Glotzer, S. C.; Murray, C. B. Evaporation-Driven Coassembly of Hierarchical, Multicomponent Networks. *ACS Nano* **2022**, *16*, 4508–4516.
- (40) Elbert, K. C.; Taheri, M. M.; Gogotsi, N.; Park, J.; Baxter, J. B.; Murray, C. B. Electron Accepting Naphthalene Bisimide Ligand Architectures for Modulation of π – π Stacking in Nanocrystal Hybrid Materials. *Nanoscale Horiz.* **2020**, *5*, 1509–1514.
- (41) Elbert, K. C.; Jishkariani, D.; Wu, Y.; Lee, J. D.; Donnio, B.; Murray, C. B. Design, Self-Assembly, and Switchable Wettability in Hydrophobic, Hydrophilic, and Janus Dendritic Ligand—Gold Nanoparticle Hybrid Materials. *Chem. Mater.* **2017**, *29*, 8737–8746.
- (42) Astruc, D.; Boisselier, E.; Ornelas, C. Dendrimers Designed for Functions: From Physical, Photophysical, and Supramolecular Properties to Applications in Sensing, Catalysis, Molecular Electronics, Photonics, and Nanomedicine. *Chem. Rev.* **2010**, *110*, 1857–1959.
- (43) Alyari, M.; Scott, R. W. J. Au Cluster-Cored Dendrimers Fabricated by Direct Synthesis and Post-Functionalization Routes. *Langmuir* **2022**, *38*, 3212–3222.
- (44) Cho, T. J.; Hackley, V. A. Assessing the Chemical and Colloidal Stability of Functionalized Gold Nanoparticles; NIST SP 1200-26; National Institute of Standards and Technology: Gaithersburg, MD, 2018, NIST SP 1200-1226.
- (45) Hähsler, M.; Nádasi, H.; Feneberg, M.; Marino, S.; Giesselmann, F.; Behrens, S.; Eremin, A. Magnetic Tilting in Nematic Liquid Crystals Driven by Self-Assembly. *Adv. Funct. Mater.* **2021**, *31*, 2101847.
- (46) Hähsler, M.; Behrens, S. Dendritic Ligands for Magnetic Suspensions in Liquid Crystals. *Eur. J. Org. Chem.* **2019**, 2019, 7820–7830.
- (47) Chen, Y.-S.; Frey, W.; Kim, S.; Homan, K.; Kruizinga, P.; Sokolov, K.; Emelianov, S. Enhanced Thermal Stability of Silica-Coated Gold Nanorods for Photoacoustic Imaging and Image-Guided Therapy. *Opt. Express* **2010**, *18*, 8867.
- (48) Woo, J. Y.; Kim, K. N.; Jeong, S.; Han, C.-S. Thermal Behavior of a Quantum Dot Nanocomposite as a Color Converting Material and Its Application to White LED. *Nanotechnology* **2010**, *21*, 495704.
- (49) Ko, J.; Jeong, B. G.; Chang, J. H.; Joung, J. F.; Yoon, S.-Y.; Lee, D. C.; Park, S.; Huh, J.; Yang, H.; Bae, W. K.; Jang, S. G.; Bang, J. Chemically Resistant and Thermally Stable Quantum Dots Prepared by Shell Encapsulation with Cross-Linkable Block Copolymer Ligands. NPG Asia Mater. 2020, 12, 19.
- (50) Sun, J.; Ma, D.; Zhang, H.; Liu, X.; Han, X.; Bao, X.; Weinberg, G.; Pfänder, N.; Su, D. Toward Monodispersed Silver Nanoparticles with Unusual Thermal Stability. *J. Am. Chem. Soc.* **2006**, *128*, 15756–15764
- (51) Badia, A.; Lennox, R. B.; Reven, L. A Dynamic View of Self-Assembled Monolayers. Acc. Chem. Res. 2000, 33, 475–481.
- (52) Transition Temperatures and Related Properties of One-Ring Systems and Two-Ring Systems without Bridging Groups; Thiem, J., Ed.; Landolt-Börnstein—Group IV Physical Chemistry; Springer-Verlag: Berlin/Heidelberg, 1992; Vol. 7a.
- (53) Diroll, B. T.; Weigandt, K. M.; Jishkariani, D.; Cargnello, M.; Murphy, R. J.; Hough, L. A.; Murray, C. B.; Donnio, B. Quantifying "Softness" of Organic Coatings on Gold Nanoparticles Using Correlated Small-Angle X-Ray and Neutron Scattering. *Nano Lett.* **2015**, *15*, 8008–8012.
- (54) Ruan, H.; Jiang, Q.; Qiu, Y.; Zhang, Y.; Liao, Y.; Xie, X. Balancing Compatibility and Gelability for High-Performance Cholesteric Liquid Crystalline Physical Gels. *Langmuir* **2023**, *39*, 771–779
- (55) Hawker, C. J.; Frechet, J. M. J. Preparation of Polymers with Controlled Molecular Architecture. A New Convergent Approach to Dendritic Macromolecules. J. Am. Chem. Soc. 1990, 112, 7638–7647. (56) Iha, R. K.; Wooley, K. L.; Nyström, A. M.; Burke, D. J.; Kade, M. J.; Hawker, C. J. Applications of Orthogonal "Click" Chemistries in the Synthesis of Functional Soft Materials. Chem. Rev. 2009, 109, 5620–5686.

- (57) Grzelczak, M.; Liz-Marzán, L. M.; Klajn, R. Stimuli-Responsive Self-Assembly of Nanoparticles. *Chem. Soc. Rev.* **2019**, *48*, 1342–1361
- (58) In, I.; Jun, Y.-W.; Kim, Y. J.; Kim, S. Y. Spontaneous One Dimensional Arrangement of Spherical Au Nanoparticles with Liquid Crystal Ligands. *Chem. Commun.* **2005**, 800.
- (59) Baek, S.-I.; Kim, S.-J.; Kim, J.-H. Measurement of Anchoring Coefficient of Homeotropically Aligned Nematic Liquid Crystal Using a Polarizing Optical Microscope in Reflective Mode. *AIP Adv.* **2015**, 5, 097170.
- (60) Lavrentovich, O. D. Transport of Particles in Liquid Crystals. *Soft Matter* **2014**, *10*, 1264–1283.
- (61) Coursault, D.; Blach, J.-F.; Grand, J.; Coati, A.; Vlad, A.; Zappone, B.; Babonneau, D.; Lévi, G.; Félidj, N.; Donnio, B.; Gallani, J.-L.; Alba, M.; Garreau, Y.; Borensztein, Y.; Goldmann, M.; Lacaze, E. Tailoring Anisotropic Interactions between Soft Nanospheres Using Dense Arrays of Smectic Liquid Crystal Edge Dislocations. *ACS Nano* **2015**, *9*, 11678–11689.
- (62) Jose, R.; Skačej, G.; Sastry, V. S. S.; Žumer, S. Colloidal Nanoparticles Trapped by Liquid-Crystal Defect Lines: A Lattice Monte Carlo Simulation. *Phys. Rev. E: Stat., Nonlinear, Soft Matter Phys.* **2014**, *90*, 032503.
- (63) Mubeena, S.; Chatterji, A. Hierarchical Self-Assembly: Self-Organized Nanostructures in a Nematically Ordered Matrix of Self-Assembled Polymeric Chains. *Phys. Rev. E: Stat., Nonlinear, Soft Matter Phys.* **2015**, 91, 032602.
- (64) West, J. L.; Glushchenko, A.; Liao, G.; Reznikov, Y.; Andrienko, D.; Allen, M. P. Drag on Particles in a Nematic Suspension by a Moving Nematic-Isotropic Interface. *Phys. Rev. E: Stat., Nonlinear, Soft Matter Phys.* **2002**, *66*, 012702.
- (65) West, J. L.; Zhang, K.; Liao, G.; Glushchenko, A. V.; Reznikov, Y.; Andrienko, D.; Allen, M. P. Mechanism of Formation of Three Dimensional Structures of Particles in a Liquid Crystal. *Mol. Cryst. Liq. Cryst.* **2004**, *410*, 83–93.
- (66) West, J. L.; Zhang, K.; Andrienko, D.; Reznikov, Y.; Glushchenko, A. Liquid Crystals as a Tool for Forming Photonic Crystals. *Proc. SPIE* **2005**, *5733*, 32.
- (67) West, J. L.; Zhang, K.; Glushchenko, A.; Andrienko, D.; Tasinkevych, M.; Reznikov, Y. Colloidal Particles at a Nematic-Isotropic Interface: Effects of Confinement. *Eur. Phys. J. E* **2006**, 20, 237–242.
- (68) Anderson, V. J.; Terentjev, E. M.; Meeker, S. P.; Crain, J.; Poon, W. C. K. Cellular Solid Behaviour of Liquid Crystal Colloids 1. Phase Separation and Morphology. *Eur. Phys. J. E* **2001**, *4*, 11–20.
- (69) Li, J.; Gauza, S.; Wu, S.-T. Temperature Effect on Liquid Crystal Refractive Indices. J. Appl. Phys. 2004, 96, 19–24.
- (70) Paik, T.; Gordon, T. R.; Prantner, A. M.; Yun, H.; Murray, C. B. Designing Tripodal and Triangular Gadolinium Oxide Nanoplates and Self-Assembled Nanofibrils as Potential Multimodal Bioimaging Probes. *ACS Nano* **2013**, *7*, 2850–2859.
- (71) Jiang, G.; Huang, Y.; Zhang, S.; Zhu, H.; Wu, Z.; Sun, S. Controlled Synthesis of Au–Fe Heterodimer Nanoparticles and Their Conversion into Au–Fe ₃ O ₄ Heterostructured Nanoparticles. *Nanoscale* **2016**, *8*, 17947–17952.
- (72) Peng, S.; Lee, Y.; Wang, C.; Yin, H.; Dai, S.; Sun, S. A Facile Synthesis of Monodisperse Au Nanoparticles and Their Catalysis of CO Oxidation. *Nano Res.* **2008**, *1*, 229–234.
- (73) Diroll, B. T.; Gogotsi, N.; Murray, C. B. Statistical Description of CdSe/CdS Dot-in-Rod Heterostructures Using Scanning Transmission Electron Microscopy. *Chem. Mater.* **2016**, *28*, 3345–3351.
- (74) Carbone, L.; Nobile, C.; De Giorgi, M.; Sala, F. D.; Morello, G.; Pompa, P.; Hytch, M.; Snoeck, E.; Fiore, A.; Franchini, I. R.; Nadasan, M.; Silvestre, A. F.; Chiodo, L.; Kudera, S.; Cingolani, R.; Krahne, R.; Manna, L. Synthesis and Micrometer-Scale Assembly of Colloidal CdSe/CdS Nanorods Prepared by a Seeded Growth Approach. *Nano Lett.* 2007, 7, 2942–2950.
- (75) Fulmer, G. R.; Miller, A. J. M.; Sherden, N. H.; Gottlieb, H. E.; Nudelman, A.; Stoltz, B. M.; Bercaw, J. E.; Goldberg, K. I. NMR Chemical Shifts of Trace Impurities: Common Laboratory Solvents,

Organics, and Gases in Deuterated Solvents Relevant to the Organometallic Chemist. *Organometallics* **2010**, *29*, 2176–2179.

TRecommended by ACS

Imaging Photon-Induced Near-Field Distributions of a Plasmonic, Self-Assembled Vesicle by a Laser-Integrated Electron Microscope

Wanting He, Dongling Ma, et al.

MARCH 30, 2023 NANO LETTERS

READ 🗹

Structure-Tunable Construction of Colloidal Photonic Composites via Kinetically Controlled Supramolecular Crosslinking

Miaomiao Li, Jintao Zhu, et al.

SEPTEMBER 10, 2022

MACROMOLECULES

READ 🗹

Fullerene-Based Nanosurfactant for the Automatic Homeotropic Alignment of Liquid Crystals

Minwook Park, Kwang-Un Jeong, et al.

MAY 01, 2023

ACS APPLIED NANO MATERIALS

READ 🗹

Symmetry-Breaking and Self-Sorting in Block Copolymer-Based Multicomponent Nanocomposites

Le Ma, Ting Xu, et al.

MAY 31, 2022

ACS NANO

READ 🗹

Get More Suggestions >